Check for updates

Received: 23 June 2023 | Revised: 4 October 2023 | Accepted: 5 October 2023

DOI: 10.1002/mrm.29898

RAPID COMMUNICATION

Magnetic Resonance in Medicine

Direct observation of NMR transverse relaxation in nanopatterned clusters of iron oxide particles

Ilhan Bok[1,2,3] | **Beth Rauch**[4] | **Alireza Ashtiani**[1] | **Aviad Hai**[1,2,3]

[1]Department of Biomedical Engineering, University of Wisconsin–Madison, Madison, Wisconsin, USA

[2]Department of Electrical and Computer Engineering, University of Wisconsin – Madison, Madison, Wisconsin, USA

[3]Wisconsin Institute for Translational Neuroengineering (WITNe), Madison, Wisconsin, USA

[4]Department of Medical Physics, University of Wisconsin – Madison, Madison, Wisconsin, USA

Correspondence
Aviad Hai, Department of Biomedical Engineering, University of Wisconsin–Madison, Madison, Wisconsin, USA.
Email: ahai@wisc.edu

Funding information
Common Fund, Grant/Award Number: DP2NS122605; National Institute of Biomedical Imaging and Bioengineering, Grant/Award Number: K01EB027184; National Institute of Neurological Disorders and Stroke; U.S. Naval Research Laboratory, Grant/Award Numbers: N00014-22-1-2371, N00014-23-1-2006; Wisconsin Alumni Research Foundation

Abstract

Purpose: We aim to verify predictions showing T_2 relaxation rate of nanoparticle clusters and its dependence on spacing, size, geometry, and pulse sequence.

Methods: We performed a laboratory validation study using nanopatterned arrays of iron oxide nanoparticles to precisely control cluster geometry and image diverse samples using a 4.7T MRI scanner with a T_2-weighted fast spin-echo multislice sequence. We applied denoising and normalization to regions of interest and estimated relative R_2 for each relevant nanoparticle array or nanocluster array. We determined significance using an unpaired two-tailed *t*-test or one-way analysis of variance and performed curve fitting.

Results: We measured a density-dependent T_2 effect ($p = 8.9976 \times 10^{-20}$, one-way analysis of variance) and insignificant effect of cluster anisotropy ($p = 0.5924$, unpaired *t*-test) on T_2 relaxation. We found negative quadratic relationships ($-0.0045[\log \tau_D]^2 - 0.0655[\log \tau_D] - 2.7800$) for single nanoparticles of varying sizes and for clusters ($-0.0045[\log \tau_D]^2 - 0.0827[\log \tau_D] - 2.3249$) for diffusional correlation time $\tau_D = r_p{}^2/D$. Clusters show positive quadratic relationships for large ($3.8615 \times 10^{-6}\ [d_{pp}/r_p]^2 - 9.3853 \times 10^{-5}\ [d_{pp}/r_p] - 2.0393$) and exponential relationships for small ($-2.0050[d_{pp}/r_p]^{0.0010}$) clusters. Calculated R_2 peak values also align well with in silico predictions (7.85×10^{-4} ms compared with 1.47×10^{-4}, 4.23×10^{-4}, and 5.02×10^{-4} ms for single iron oxide nanoparticles, 7.88×10^{-4} ms compared with 5.24×10^{-4} ms for nanoparticle clusters).

Conclusion: Our verification affirms longstanding in silico predictions and demonstrates aggregation-dependent behavior in agreement with previous Monte Carlo simulation studies.

KEYWORDS

cluster, FSEMS, MRI, nanoparticle, relaxation, transverse

This is an open access article under the terms of the Creative Commons Attribution License, which permits use, distribution and reproduction in any medium, provided the original work is properly cited.

© 2023 The Authors. *Magnetic Resonance in Medicine* published by Wiley Periodicals LLC on behalf of International Society for Magnetic Resonance in Medicine.

1 | INTRODUCTION

T_2 relaxation in MRI and readouts from other recently evolving imaging modalities such as magnetic particle imaging[1,2] and optically detected MR,[3,4] are all modulated by multiplexed, concentration-dependent features of magnetic tracers, sensors, and substrates.[2,4,5] In clinical setting, superparamagnetic iron oxide nanoparticles (SPIONs) can specifically serve as the agent of choice for tissue contrast enhancement[6–8] and perfusion-dependent structural readouts.[7–9] SPIONs usually act as purely passive isotropic injectable agents, demonstrating an inherent ability to accumulate in different tissue types. Examples include hepatic lumen cells,[10–12] splenic red pulp cells,[10,13] gliosarcoma,[14] and many more.[5] These provide powerful diagnostic tools for detecting structural and tissue manifestations of pathologies such as cirrhosis,[10] liver cancer,[10,11] spleen cancer,[15] and brain disorders.[16] In addition to static image contrast enhancement, newly emerging responsive SPION-based sensors rely on specialized chemical coating to enable dynamic functional readouts of biophysical and biochemical components.[17–19] Examples include SPIONs conjugated with calmodulin and its target peptides[20,21] or C2 domains of synaptotagmin[22] as calcium-responsive MRI contrast agents; engineered monoaminergic binding peptide domains for sensing neurotransmitters[23]; and more.[24–27] Moreover, other types of injectable nanoparticles, nanostructures, and molecular probes offer aggregation-based sensing and modulation of electric fields[28–32] and biochemical processes[33–35] with particular uses in neuroscience and neurology.[36] The spatial distribution and related aggregation attributes of magnetic particles are important to both static and dynamic contrast enhancement, as the final 3D scaling factor, arrangement, and distribution of tracers can affect image quality, contrast, SNR, and sensitivity to analytes. This highlights the importance of precise prediction of SPION aggregation and corresponding MRI signal changes accompanying their nanoscale spatial organization.

Theoretical predictions of changes in relaxation rate (R_2) due to SPION aggregation reveal a dependence on particle size, geometry, and anisotropy.[37–41] Random walk simulations of water molecules diffusing in proximity to SPIONs suggest these nonlinearities also depend on scan parameters.[40,41] Specifically, spin phase dispersion surrounding small nanoparticles are governed by classic outer sphere theory[37] in what is termed the simple motional averaging regime. This effect plateaus and decreases for larger nanoparticles using spin-echo pulse sequences with large enough TE in what is termed the slow motion regime.[42] For single nanoparticles of radius r_p in medium with self-diffusion constant (D), the transition between these two regimes is represented by the diffusional correlation time ($\tau_D = {r_p}^2/D$) and is predicted to occur at a point inversely proportional to the angular frequency shift at the particle surface ($\Delta\omega_r$).[43] More recent models attempt to describe this relationship for clustered SPIONs in the context of aggregation-based MRI sensing[41] reporting peak R_2 transition value between the motional averaging regime and slow motion regime of $85.59\,s^{-1}$ at $\tau_D = 5.02\times10^{-4}$ ms for single particles/dots and $87.31\,s^{-1}$ at $\tau_D = 5.24\times10^{-4}$ ms for 3D isotropic clusters. Chemical exchange models of diffusion[38] demonstrated comparable peak R_2 value of $0.45\,s^{-1}$ for echo spacing $\tau_{CP} = 0.5$ ms and $\Delta\omega_r = 472$ rad/s, at $\tau_D = 0.15$ ms ($\tau_D/\tau_{CP} = 1.97$) with a volume fraction (v) of 0.005: Normalizing by v yields $\tau_D = 1.47\times10^{-4}$. The chemical exchange model posits that water molecules either diffuse past iron oxide nanoparticles ("outer sphere") or contact and bind them ("inner sphere") and that flux between these two states influences diffusion-related T_2 relaxation behavior. A few measurements have supported these studies indirectly,[44–48] but a piecewise ground-truth experimental validation of this effect has not yet been performed.

Here we use precise nano-scale lithography of SPION clusters to provide direct experimental observation of the concept of significant alterations in R_2 due to aggregation. By extracting R_2 values from MRI measurements of nanofabricated arrays of SPION clusters, we demonstrate peak diffusion time correlating with model predictions, with peak τ_D measured at 7.85×10^{-4} ms for single particles. Peak τ_D for isotropic 2D clusters was 7.88×10^{-4} ms and similarly correlated. Our results present a first validation and agreement with long-standing theoretical predictions of the behavior of iron oxide nanoparticles and provide a novel protocol with broad implications on the analyses and development of MRI contrast agents and aggregation-based sensors and modulators.

2 | METHODS

2.1 | Finite element analyses of magnetic fields

Magnetic field profiles of SPION clusters were simulated using COMSOL Multiphysics 6.0 (COMSOL Inc., Stockholm, Sweden). The Magnetic Fields (mf) module was used to emulate nanoparticle arrays under a 4.7T B_0 bias field applied along the y-direction within a hexagonal simulation arena with periodic boundary condition. The Ampere's Law boundary condition with a B-H curve magnetization model was applied on low carbon steel magnetite particles (COMSOL Materials Library) surrounded by CSF (relative electrical permittivity $\varepsilon_r = 81.2$, electrical conductivity $\sigma = 4.8$ S/m). A Job Configurations node was

15222594, 2024, 2, Downloaded from https://onlinelibrary.wiley.com/doi/10.1002/mrm.29898 by Centura Health Library, Wiley Online Library on [29/11/2023]. See the Terms and Conditions (https://onlinelibrary.wiley.com/terms-and-conditions) on Wiley Online Library for rules of use; OA articles are governed by the applicable Creative Commons License

used to perform a parametric sweep of interparticle distance (d_{pp}) to particle radius (r_p) ratio (d_{pp}/r_p), ranging from 3 to 40 in 0.1 increments. The resultant magnetic field values were processed using *Python 3.7* as follows: Values were weighted by mesh element size within a region of radius $\frac{1}{2}*d_{pp}$ at the center, left, or right region of the nanoparticle cluster, and an origin-centered circle with radius $2*d_{pp}$ was used to define the FOV of the cluster. Statistical traces were further processed and visualized using *MATLAB* R2022a (MathWorks, Inc., Natick, MA, USA). A moving average centered between the current and previous elements with a sliding window of four frames was used to smooth the mean and SD for all field traces against d_{pp}/r_p. Averages were truncated at endpoints where there were not enough elements to fill the moving mean window.

2.2 | Nanostructure fabrication

We used electron beam nanolithography to create nanopatterned iron oxide arrays (Figure 1A). A silicon N-type phosphorus doped <100> 1–10 Ω·cm 380 µm single-side polished wafer (Cat. Number 695; UniversityWafer, Boston, MA, USA) was spin-coated with poly methyl-methacrylate 495 A4 photoresist (Kayaku Advanced Materials Inc., Westborough, MA, USA) at 4000 rpm for 45 s. After verifying a film thickness of 185 nm (F20 Reflectometer; Filmetrics, Inc., San Diego, CA, USA), the wafer sample was baked on a hotplate at 180°C for 90 s. The baked wafer was diced into 10 × 10 mm chips and patterned using an Elionix ELS G-100 electron beam lithography system (Elionix Inc., Tokyo, Japan) using the parameters given in Table 1. Samples were developed at room temperature in 1:3 methyl isobutyl ketone (Cat. Number M2131; Thermo Fisher Scientific Inc., Waltham, MA, USA):isopropanol (MIBK:IPA) for 60 s and rinsed first with IPA, then with deionized (DI) water. After inspecting the consistency of developed samples (Figure S1) using a Zeiss LEO 1530-1 field emission scanning electron microscope (SEM; Carl Zeiss AG, Oberkochen, Germany), a custom-built electron beam metal evaporator was used to deposit a 30-nm layer of iron oxide at 0.2 Å/s at room temperature (~20°C) and relative humidity of 23% or less. Samples were lifted off in room temperature acetone with gentle agitation to prevent re-adhesion of iron. Completed samples were rinsed first with IPA, then with DI water. Structures were visually inspected for cleanliness and consistency after each processing step using an Olympus BX51WI Upright Fluorescent Microscope (Olympus, Tokyo, Japan).

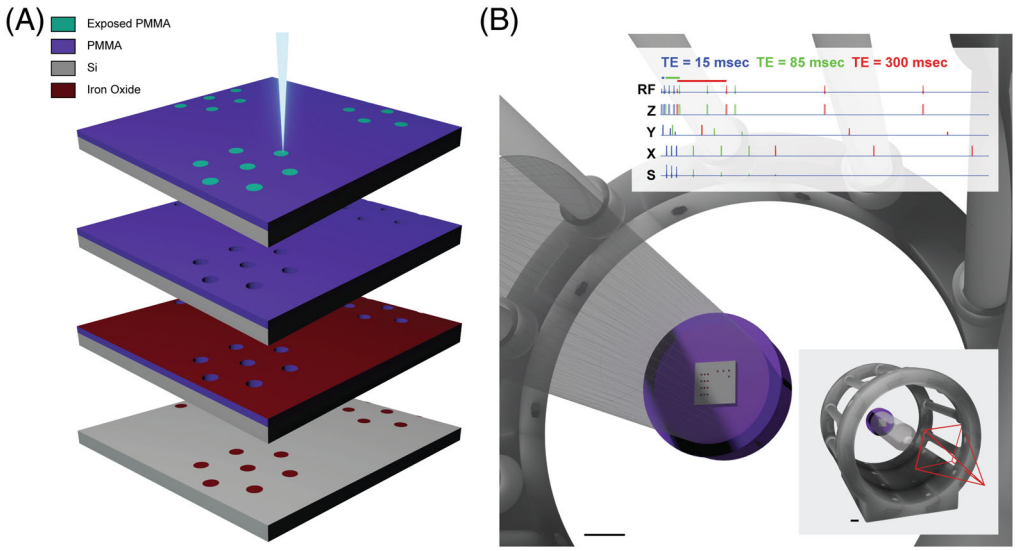

FIGURE 1 Iron oxide nanoparticle cluster fabrication and MR scan schematic. (A, from top to bottom) A layer of poly methyl-methacrylate is spin-coated onto a silicon substrate and patterned using electron beam lithography. The layer is then developed using a 1:3 mixture of methyl isobutyl ketone: isopropanol, coated with an ultrathin layer of iron oxide using electron beam metal evaporation, then lifted off using room-temperature acetone with gentle agitation. (B) A scanning procedure schematic showing the iron oxide chip attached to the inside of a conical tube, placed into a birdcage coil (scale bar = 10 mm) and scanned using multislice fast spin echo (upper right) with variable TE. Values from 15 to 300 ms in 15 ms increments were recorded. An image using a TE of 85 ms was chosen for further analysis (see Figure 4). The full configuration is shown on the bottom right, with the perspective seen in the full panel shown as a red prism (scale bar = 10 mm).

15222594, 2024, 2, Downloaded from https://onlinelibrary.wiley.com/doi/10.1002/mrm.29898 by Centura Health Library, Wiley Online Library on [29/11/2023]. See the Terms and Conditions (https://onlinelibrary.wiley.com/terms-and-conditions) on Wiley Online Library for rules of use; OA articles are governed by the applicable Creative Commons License

TABLE 1 Parameters used for electron beam lithography patterning of Si/PMMA substrate.

Array type	Density/anisotropy	Size/cluster
Field size (μm)	250	250
Dot number	500 000	500 000
Exposure (μC/cm^2)	800	(800, 1600, 2400)
Feed pitch	10	10
Scan pitch	10	10
Beam current (nA)	2	10
Exposure time (μs/dot)	0.10	(0.02, 0.04, 0.06)
Matrix size (μm × μm)	100.0 × 100.0 (density)	100.0 × 100.0
	122.5 × 70.0 (anisotropy)	

TABLE 2 Parameters used for MR scans of iron oxide nanoparticle arrays.

Scan parameters	Density and anisotropy arrays	Size and spacing arrays
Pulse sequence	FSEMS	FSEMS
Field strength (T)	4.7	4.7
TE (ms)	68	85
TR (ms)	4000	5000
Voxel size (μm × μm)	78.1 × 79.4	70.3 × 71.4
Slice thickness (μm)	700	400
Number of averages	10	12

2.3 | Fast spin-echo multislice MRI T_2 scans

Nanofabricated samples were epoxied (Cat. Number 078143-14210; R.S. Hughes Co., Inc., Sunnyvale, CA, USA) with the patterned side facing up on a cylindrical high density polyethylene surface (radius = 10 mm, height = 10 mm), which was itself epoxied into a 50-mL centrifuge tube cap, and the entire phantom tube was filled with reagent-grade DI water. Images were acquired using fast spin-echo multislice T_2-weighted scans (Table 2) on an Agilent 4.7T horizontal-bore MRI/MRS system housing a 72-mm inner diameter Agilent/Varian quad birdcage volume coil (#S190888200 108/38 1H 200 MHz; Varian Medical Systems, Inc., Palo Alto, CA, USA) (Figure 1B). For density-dependent and anisotropy-dependent samples (Figure 2), we used TE = 68 ms, TR = 4000 ms, and a voxel size of 78.1 × 79.4 μm with a slice thickness of 700 μm and $N = 10$ averages. For arrays of varying nanoparticle size and nanoparticle clusters, scans used TE = 85 ms, TR = 5000 ms, and a voxel size of 70.3 × 71.4 μm with a slice thickness of 400 μm and $N = 12$ averages.

2.4 | Quantifications of density-dependent MR intensity trends

Sixteen-bit DICOM (Digital Imaging and Communications in Medicine) MR images were thresholded below a value of 1.47×10^4. For density-dependent DICOM images, *ImageJ* (National Institutes of Health, Bethesda, Maryland, USA) was used for background correction assuming a light background and a rolling ball radius of 50 px. A 4 px × 4 px selection window was applied to each density. Raw optical images were thresholded at 6.02×10^4, and a polygonal selection was manually applied to each region of interest (ROI). For both image analyses, a least-squares linear fit of iron oxide nanoparticle concentration to median pixel value was used to determine R_2.

2.5 | Quantifications of relative R_2 trends

To determine R_2 for each ROI, *Python* 3.7 was used to curve fit a Gaussian probability density function to a reference histogram of background pixel intensities according to:

15222594, 2024, 2, Downloaded from https://onlinelibrary.wiley.com/doi/10.1002/mrm.29898 by Centura Health Library, Wiley Online Library on [29/11/2023]. See the Terms and Conditions (https://onlinelibrary.wiley.com/terms-and-conditions) on Wiley Online Library for rules of use; OA articles are governed by the applicable Creative Commons License

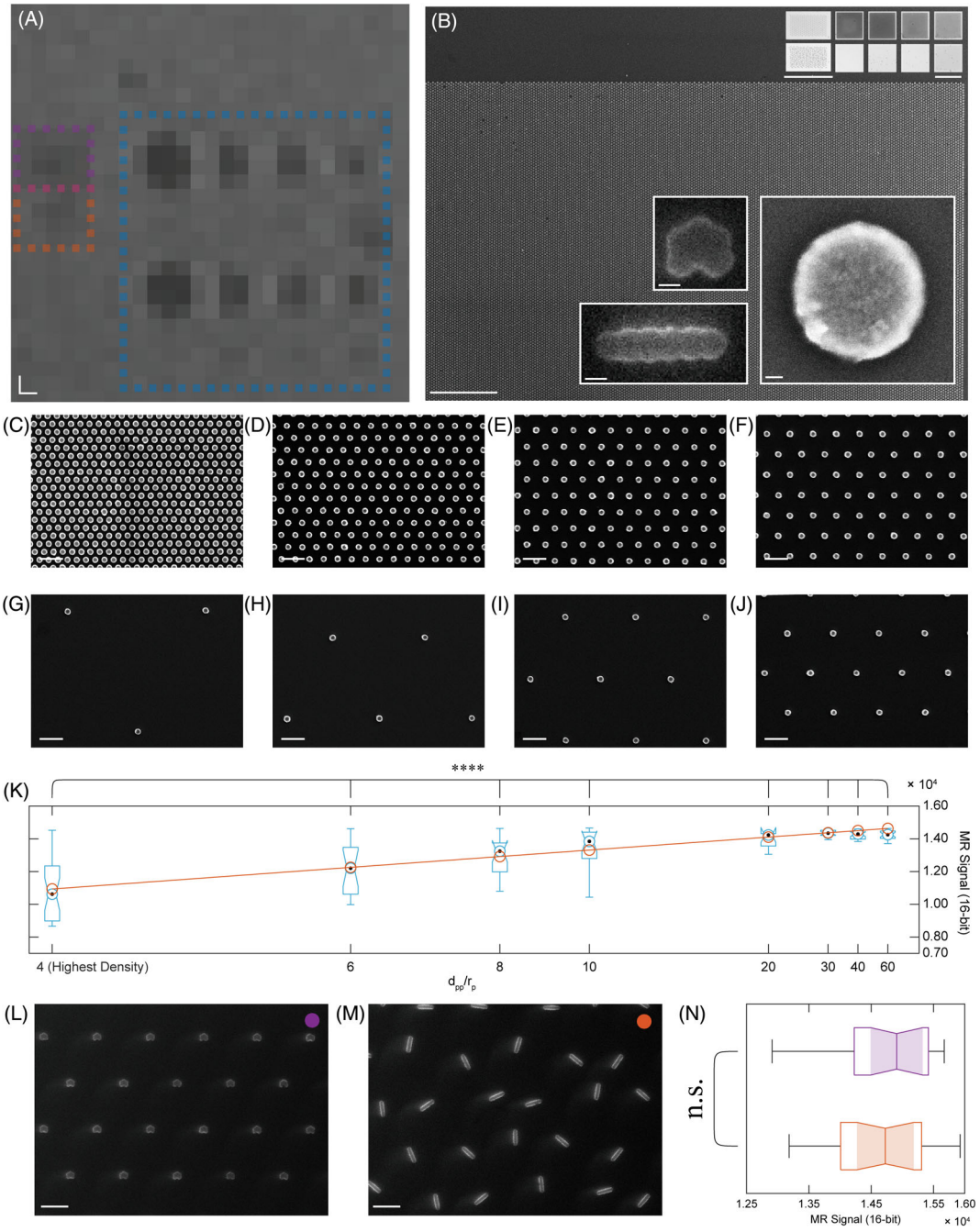

FIGURE 2 Magnetic resonance (MR) and scanning electron microscopy (SEM) images of nanopatterned iron oxide arrays reveal density dependence and a non-significant effect of anisotropy on R_2. (A) T_2-weighted fast spin-echo multislice MR images reveal a density-dependent response to $100 \times 100\ \mu m^2$ nanopatterned iron oxide arrays (diameter = 200 nm, scale bar = $200 \times 200\ \mu m$). Blue, violet, and orange boxes denote regions corresponding to (C)–(J), (L), and (M), respectively. (B) Viewing the nanopatterned iron oxide arrays under SEM (main panel, $d_{pp}/r_p = 4$, scale bar = 10 μm) and optical microscopy (upper insets, left column scale bar = 50 μm, other columns scale bar = 100 μm) shows density-dependent darkening as well as differing anisotropy for chains (bottom-left inset, scale bar = 200 nm) and clusters (upper-left inset, scale bar = 200 nm). A single-nanoparticle SEM shows consistency and uniformity when approaching single-atom resolution (right inset, scale bar = 30 nm). SEM scans of interparticle spacing to radius (d_{pp}/r_p) ratios of 4 (C), 6 (D), 8 (E), 10 (F), 60 (G), 40 (H), 30 (I), and 20 (J) in the same order as (A) and (B) are shown below (scale bar = 1 μm). (K) Box plot of relative MR signal intensity versus d_{pp}/r_p. Black dots denote the median; notches denote bounds of statistical significance; and whiskers denote outlier thresholds (from $Q1 - W \times [Q3 - Q1]$ to $Q3 + W \times [Q3 - Q1]$ where $W = 1.5$). The orange line and data points represent a linear curve fit to the medians of each d_{pp}/r_p ($m = 1.5850 \times 10^4$ [MR signal]/$[d_{pp}/r_p]^{-1}$, $b = 2.7895 \times 10^4$ [MR signal]; $p = 8.9976 \times 10^{-20}$, **** $p < 0.0001$, one-way analysis of variance, $R_2 = 0.9442$). SEM images of nanoparticle clusters (L) and randomly oriented nanochains (M) (scale bar = 2 μm). (N) Pixel intensity analysis of both regions reveals no significant effect of anisotropy on R_2 ($p = 0.5924$, unpaired t-test).

15222594, 2024, 2, Downloaded from https://onlinelibrary.wiley.com/doi/10.1002/mrm.29898 by Centura Health Library, Wiley Online Library on [29/11/2023]. See the Terms and Conditions (https://onlinelibrary.wiley.com/terms-and-conditions) on Wiley Online Library for rules of use; OA articles are governed by the applicable Creative Commons License

TABLE 3 Gaussian blurring parameters and corresponding SNR values for R_2 plots in Figure 4.

Analysis type	Region-of-interest size	Gaussian kernel σ	μ noise (s^{-1})	σ noise (s^{-1})	SNR (dB)
Single	3 × 3	1	−2.071	1.071×10^{-3}	44.530
Cluster	2 × 2	0	−2.076	2.173×10^{-3}	24.983
Small clusters	2 × 4	0	−2.074	3.349×10^{-3}	25.134
Small clusters Gaussian blurring	2 × 2	2	−2.070	2.652×10^{-4}	43.198
Large clusters	2 × 3	2	−2.070	3.800×10^{-4}	37.429

$$\boldsymbol{w} = \text{normalpdf}(\min(\mu_B, \boldsymbol{S}), \sigma_B) \quad (1)$$

where $\boldsymbol{S}$ is the raw MR signal matrix; μ_B is the mean background brightness; σ_B is the SD of background brightness; and normalpdf is probability density function of the Gaussian distribution. We then shifted this mean by a constant value for each ROI to compensate for background field inhomogeneities before calculating R_2 values. The resultant pixel weight vectors ($\boldsymbol{w}$) were used to find T_2 values for each voxel ($\boldsymbol{S_{T2}}$) using:

$$\boldsymbol{S_{T2}} = \left(1 - \boldsymbol{w}\sigma_B\sqrt{2\pi}\right) * \boldsymbol{S} \quad (2)$$

The output was processed by a Gaussian filter to remove noise (see Table 3 for σ parameter and resultant SNR values for each ROI type) and estimated relative R_2 with:

$$\mu_{R2} = \text{mean}\left(\log\left(\boldsymbol{S_{T2}}\right)^{-1}\right) \quad (3)$$

where μ_{R2} is the mean relative R_2 over each ROI normalized to plots of simulated relaxivity changes with minor variations between the corresponding plots.[1]

3 | RESULTS

3.1 | T_2 measurements of iron oxide nanoparticle arrays reveal density-dependent and anisotropy-independent behavior

T_2-weighted fast spin-echo multislice MR images of 200-nm nanopatterned iron oxide particles affirm a density-dependent (particles per unit area) response in $100 \times 100\,\mu m^2$ arrays and nonsignificant effect of structure anisotropy (Figure 2A). SEMs (Figure 2B, main panel and lower insets) and optical microscopy (Figure 2B, upper insets) of nanopatterned particles verify consistent linear density-dependent signal decrease (Figure S2) and variable anisotropy for nanoparticle chains and clusters (Figure 2B, upper left, optical; bottom left, SEM). A single-nanoparticle SEM shows structural uniformity when at near single-atom resolution (Figure 2B, lower right inset). SEMs of interparticle spacing to radius (d_{pp}/r_p) ratios of 4, 6, 8, 10, 60, 40, 30, and 20 are shown in Figure 2C–J, respectively, and in the same order as Figure 2A,B. Comparing MRI voxel intensity versus $(d_{pp}/r_p)^{-1}$ reveals a density-dependent response (Figure 2K). Shown in Figure 2K are black dots denoting the median, notches denoting bounds of statistical significance, and whiskers denoting outlier thresholds from $Q1–1.5 \times (Q3–Q1)$ to $Q3 + 1.5 \times (Q3–Q1)$, where $Q1$ is the first quartile or 25th percentile, $Q3$ is the third quartile or 75th percentile, $(Q3–Q1)$ is the interquartile range, and $1.5 \times (Q3–Q1)$ is the outlier cutoff threshold. The orange curve in Figure 2K and corresponding data points represent a linear curve fit to the medians of each $(d_{pp}/r_p)^{-1}$ ($m = 1.5850 \times 10^4$ (MR signal)/$(d_{pp}/r_p)^{-1}$, $b = 2.7895 \times 10^4$ (MR signal) ($p = 8.9976 \times 10^{-20}$, **** = $p < 0.0001$, one-way analysis of variance). Minor variations in brightness exist at lower densities (d_{pp}/r_p ranging between 30 and 60), independent of background gradient correction. SEM images of compact nanoparticle clusters and randomly oriented and positioned nanoparticle chains (Figure 2L,M, respectively) confirm the consistency of our cluster fabrication method. MRI signal brightness of both regions reveal no significant effect of anisotropy on T_2 decay (Figure 2N; $p = 0.5924$, unpaired t-test). Based on these verifications of uniformly dense arrays of single nanoparticles, we turned to finite element analysis to predict the effect of nonuniform aggregation on magnetic fields.

3.2 | Finite element analysis of hexagonal nanoparticle clusters affirms proximity-dependent field enhancement

We used finite element analysis to quantify B_0-induced magnetization in single nanoparticles (Figure 3A), and clusters of nanoparticles with $d_{pp}/r_p = 40$ (Figure 3B), $d_{pp}/r_p = 20$ (Figure 3C), $d_{pp}/r_p = 10$

[1]Resources for quantifying R2 relaxation from 2D clusters and arrays of SPIONs are available at https://github.com/hailab-uw/2D_SPIO_R2

15222594, 2024, 2, Downloaded from https://onlinelibrary.wiley.com/doi/10.1002/mrm.29898 by Centura Health Library, Wiley Online Library on [29/11/2023]. See the Terms and Conditions (https://onlinelibrary.wiley.com/terms-and-conditions) on Wiley Online Library for rules of use; OA articles are governed by the applicable Creative Commons License

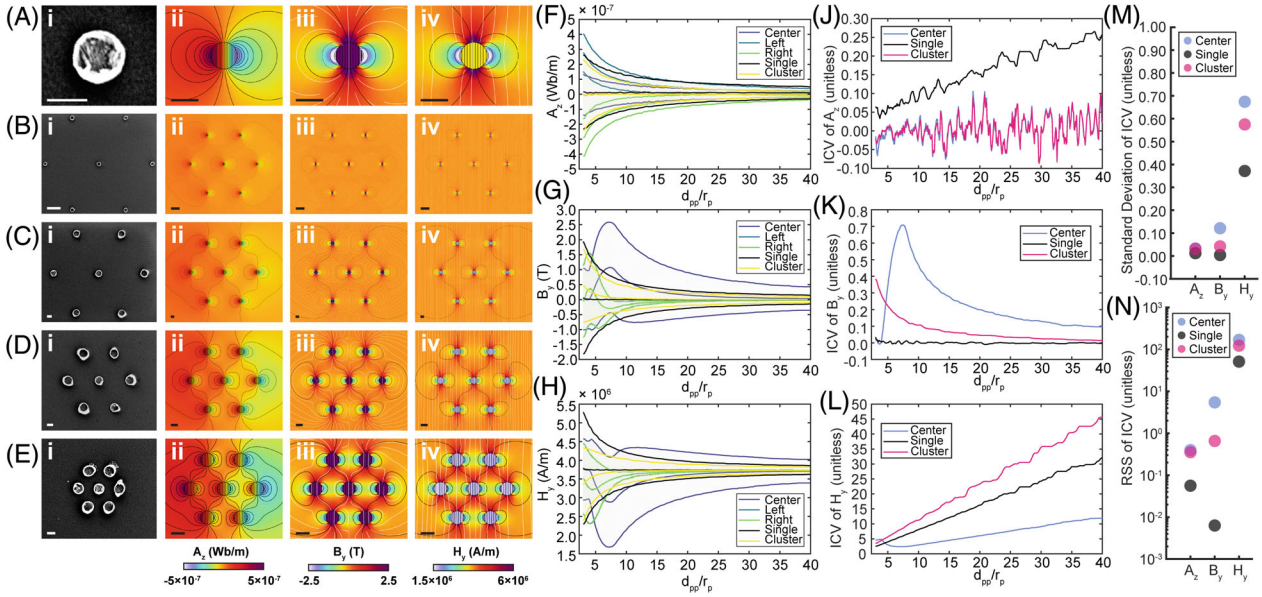

FIGURE 3 Finite element analysis demonstrates highly diverse magnetic fields in proximity to nanoparticle clusters compared with single nanoparticles. Data for nanoparticles (A), nanoparticle clusters with $d_{pp}/r_p = 40$ (B), $d_{pp}/r_p = 20$ (C), $d_{pp}/r_p = 10$ (D), and $d_{pp}/r_p = 5$ (E) (nanoparticle diameter = 200 nm; scale bar = 200 nm except [B], where scale bar = 1 μm). SEM (A[i]–E[i]), magnetic vector potential z-component $\mathbf{A}_z$ (A[ii]–E[ii]), magnetic flux density y-component $\mathbf{B}_y$ (A[iii]–E[iii]), magnetic field intensity y-component $\mathbf{H}_y$ (A[iv]–E[iv]) of various d_{pp}/r_p. Corresponding running-average ($n = 4$) mean and SD of a nanoparticle and center, left, right, and entire cluster are shown for $\mathbf{A}_z$ (F), $\mathbf{B}_y$ (G), and $\mathbf{H}_y$ (H). Changes in inverse coefficient of variation (ICV) for varying interparticle distance to particle radius ([F]–[H]). The ICV, defined as the mean divided by the SD of field values around particles in the simulation arena, for magnetic vector potential z-component A_z (J), magnetic flux density y-component B_y (K), and magnetic field intensity y-component H_y (L) of d_{pp}/r_p ranging from 3.0 to 40.0 in increments of 0.1. Although the ICV increases relatively linearly for single particles, changes are more stochastic or highly nonlinear for the entire cluster, particularly the nanoparticle at the center of the cluster. Comparing the residual sum of squares (RSS) (M) and the adjusted SD of the ICV versus magnetic field type (N) shows that single nanoparticles are less variable than clusters and center nanoparticles.

(Figure 3D), and $d_{pp}/r_p = 5$ (Figure 3E). SEM reference images (Figure 3A[i]–E[i]) show proof of principle structures for simulations of magnetic vector potential (Figure 3A[ii]–E[ii]), magnetic flux density (Figure 3A[iii]–E[iii]), and magnetic field intensity (Figure 3A[iv]–E[iv]) of varying cluster values of d_{pp}/r_p. Corresponding running-average mean and SD of fields across a single nanoparticle (Figure 3F–H, black curves), from the center, left, and right regions of a single nanoparticle (Figure 3F–H, purple, blue, green curves, respectively), and across the entire cluster (Figure 3F–H, yellow) are shown for magnetic vector potential z-component ($\mathbf{A}_z$, Figure 3F), magnetic flux density y-component ($\mathbf{B}_y$, Figure 3G), and magnetic field intensity y-component ($\mathbf{H}_y$, Figure 3H). The inverse coefficient of variation (ICV), defined as the mean field amplitude divided by the SD (μ/σ) surrounding nanoparticles in the simulation arena (Figure 3J–L), shows greater variability for clustered nanoparticles compared with single nanoparticles under the same simulation conditions, demonstrating a clear aggregation-related effect. Specifically, the residual sum of squares (RSS) for single nanoparticles for $\mathbf{A}_z$, $\mathbf{B}_y$, and $\mathbf{H}_y$ are 0.0561, 0.0063, and 51.0562, whereas for the center nanoparticle in a cluster they are 0.3968 ($7.0733 \times \mathrm{RSS}_{\mathrm{single}}$), 5.4398 (862.6164), and 168.2382 (3.2952), and for the whole cluster the values are 0.3537 (6.3044), 0.6542 (103.7460), and 122.3860 (2.3971) (Figure 3M). The larger RSS for clusters affirms that iron oxide nanoparticle clusters exhibit highly variable fields compared with single nanoparticles. Although ICV increases relatively linearly for single nanoparticles, changes are more stochastic or highly nonlinear for the entire cluster and single nanoparticles at the cluster center. Subtracting the line of best fit yields SDs for $\mathbf{A}_z$, $\mathbf{B}_y$, and $\mathbf{H}_y$ of 0.0123, 0.0041, and 0.3715 for single nanoparticles, 0.0327 ($2.6596 \times \sigma_{\mathrm{single}}$), 0.1213 (29.3703), and 0.6743 (1.8153) for center nanoparticles, and 0.0309 (2.5109), 0.0421 (10.1856), and 0.5751 (1.5483) for the whole cluster (Figure 3N). Of note are ICVs for magnetic flux density (Figure 3K), which fluctuate from −0.0099 at $d_{pp}/r_p = 20.9$ to 0.0345 at $d_{pp}/r_p = 3.0$ for isolated single iron oxide nanoparticles compared with fluctuations from −0.0077 at $d_{pp}/r_p = 3.6$ to 0.7086 at $d_{pp}/r_p = 7.3$ for center iron oxide nanoparticles. These simulations therefore predict that aggregation of nanoparticles produces fields that show asymptotic behavior with increasing d_{pp}/r_p

15222594, 2024, 2, Downloaded from https://onlinelibrary.wiley.com/doi/10.1002/mrm.29898 by Centura Health Library, Wiley Online Library on [29/11/2023]. See the Terms and Conditions (https://onlinelibrary.wiley.com/terms-and-conditions) on Wiley Online Library for rules of use; OA articles are governed by the applicable Creative Commons License

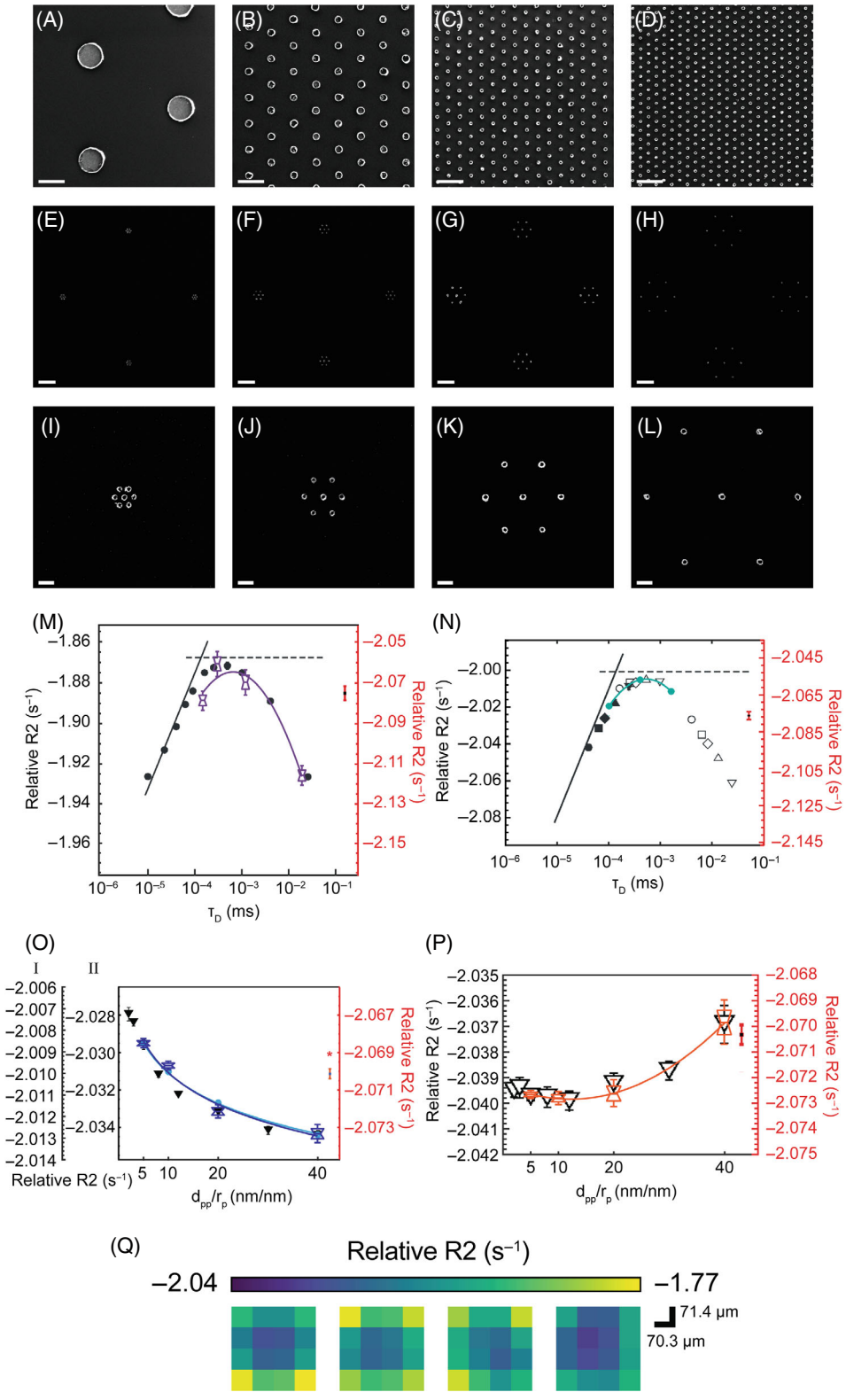

FIGURE 4 Scanning electron microscope (SEM) images and corresponding MR R_2 plots of signal and noise show trends in agreement with previous Monte Carlo simulations. Shown are SEMs of different nanopatterned iron oxide arrays with $d_{pp}/r_p = 10$ of sizes of 800 nm (A), 200 nm (B), 100 nm (C), and 70 nm (D) (scale bar = 1 μm). Below are SEMs of four representative nanoparticle clusters of $r_p = 50$ nm and $d_{pp}/r_p = 5$ (E), $d_{pp}/r_p = 10$ (F), $d_{pp}/r_p = 20$ (G), and $d_{pp}/r_p = 40$ (H) (scale bar = 2 μm), corresponding to magnified panels (I–L, scale bar = 400 nm). Relative T_2 relaxation rates (R_2) (left axis) and noise levels (right axis) normalized to previous simulations show agreement in diffusional correlation time $\tau_D = r_p{}^2/D$ for single nanoparticles (*M*) (A–D) and nanoparticle clusters of nanoparticles (*N*) (E, inset panel I). (O) Relative R_2 values from nanoparticle clusters of small nanoparticles ($r_p = 35$ nm or 50 nm as in [E]–[H] [inset panels (I)–(L)]), where I corresponds to raw data (light blue); II corresponds to Gaussian blurred data (navy blue); and * denotes noise level after Gaussian blurring. (P) Large nanoparticles ($r_p = 400$ nm patterned like panels [E]–[H] [I-1], size differs) also show R_2 trends versus d_{pp}/r_p in agreement with Monte Carlo simulations. When present, lines denote the median; notches denote bounds of statistical significance; and whiskers denote outlier thresholds from $Q1–1.5\times(Q3–Q1)$ to $Q3+1.5\times(Q3–Q1)$, where *Q1* is the first quartile or 25th percentile; *Q3* is the third quartile or 75th percentile; $(Q3–Q1)$ is the interquartile range; and $1.5\times(Q3–Q1)$ is the outlier cutoff threshold. (Q) The corresponding MRI regions of interest for (M) after conversion to R_2.

15222594, 2024, 2, Downloaded from https://onlinelibrary.wiley.com/doi/10.1002/mrm.29898 by Centura Health Library, Wiley Online Library on [29/11/2023]. See the Terms and Conditions (https://onlinelibrary.wiley.com/terms-and-conditions) on Wiley Online Library for rules of use; OA articles are governed by the applicable Creative Commons License

and are spatially diverse compared with those of single nanoparticles.

3.3 | MR scan-derived R_2 trends agree with Monte Carlo simulations

To corroborate nanoparticle aggregation–dependent and nanoparticle size–dependent field effects predicted in theory, we performed MRI of varying nanopatterned iron oxide cluster arrays (Figure 4). SEMs of constant $d_{pp}/r_p = 10$ and variable nanoparticle sizes of 800 nm (Figure 4A), 200 nm (Figure 4B), 100 nm (Figure 4C), and 70 nm (Figure 4D) demonstrate consistent uniformity of nanoparticles and nanoparticle clusters (Figure 4A–L). Four representative nanoparticle clusters (and corresponding zoomed insets) with nanoparticle diameter of 100 nm and $d_{pp}/r_p = 5$ (Figure 4E,J), $d_{pp}/r_p = 10$ (Figure 4F,J), $d_{pp}/r_p = 20$ (Figure 4G,K), and $d_{pp}/r_p = 40$ (Figure 4H,L) are shown. Our R_2 analyses show agreement in diffusional correlation time $\tau_D = r_p^2/D$ for single nanoparticles (Figure 4M; corresponding SEMs in Figure 4A–D) and nanoparticle clusters (Figure 4N; see Figures 3E and 4E) and d_{pp}/r_p for clusters of small nanoparticles ($r_p = 35$ nm or 50 nm; Figure 4O; see Figure 4E–H) and clusters of large nanoparticles ($r_p = 400$ nm; Figure 4P; see Figure 3B–E). When present, lines denote the median; notches denote bounds of statistical significance; and whiskers denote outlier thresholds from $Q1–1.5\times(Q3–Q1)$ to $Q3+1.5\times(Q3–Q1)$, where $Q1$ is the first quartile or 25th percentile, $Q3$ is the third quartile or 75th percentile, $(Q3–Q1)$ is the interquartile range, and $1.5\times(Q3–Q1)$ is the outlier cutoff threshold. Shown in Figure 4Q are corresponding MRI ROIs for panel (m) after conversion to R_2. We found negative quadratic relationships ($-0.0045[\log \tau_D]^2–0.0655[\log \tau_D]–2.7800$) (Figure 4M) for single nanoparticles of varying sizes and for clusters ($-0.0045[\log \tau_D]^2–0.0827[\log \tau_D]–2.3249$) (Figure 4N) for varying diffusional correlation time $\tau_D = r_p^2/D$. Small clusters show changes smaller than the background noise level, which we fit quadratically ($3.2046\times10^{-6}\ [d_{pp}/r_p]^2–2.6204\times10^{-4}\ [d_{pp}/r_p]–2.0075$), inverse quadratically ($-7.9436\times10^{-7}\ [d_{pp}/r_p]^{-2}+6.4888\times10^{-5}\ [d_{pp}/r_p]^{-1}–0.4981$) and exponentially ($-2.0050[d_{pp}/r_p]^{0.0010}$) (Figure 4O). We applied Gaussian filtering to reduce noise in this ROI and determined that the percent change in signal remained consistent (−0.2097% to −0.2382% [Figure 4O]; see Table 3 for SNR values). We additionally found that large clusters show positive quadratic relationships well above noise level ($3.8615\times10^{-6}\ [d_{pp}/r_p]^2–9.3853\times10^{-5}\ [d_{pp}/r_p]–2.0393$) (Figure 4P) in agreement with previous Monte Carlo simulation studies.[40,41]

4 | DISCUSSION AND CONCLUSIONS

Here we leveraged nano-scale lithography to precisely pattern clusters of iron oxide nanoparticles and quantify their R_2 using fast spin-echo multislice MR scan data. We found nonlinear polynomial R_2 dependence for both single and diversely clustered iron oxide dots with varying interparticle distance and particle radius. Furthermore, we reported an exponential aggregation-dependent relationship between interparticle distance and particle radius, verified by nonlinear least squares trust region reflective fit strategy. A 2D array of SPIONs situated on a planar silicon surface also primarily affects field perturbations for water molecules diffusing near the plane of the nanoparticle cluster array, which may help explain relatively low SNR for exponentially fitted small nanoparticles without Gaussian filtering. To characterize magnetic field behavior for a continuum of varying interparticle spacings for nanoparticle clusters, we analyzed magnetic field maps from our finite element nanoparticle cluster model and found increasing variability quantified by both ICV and RSS with decreasing interparticle distance to particle radius ratio (d_{pp}/r_p). We note that while we investigated T_2 relaxation effects for nanoparticles with radius as small as 35 nm, some clinically used SPIONs can be as small as 4 nm.[6] Earlier theoretical work shows that MNPs below 10 nm in diameter are expected to continue trends predicted by microscopic outer sphere theory.[37] Extrapolating our experimental results yields a similar decline in the form of relative R_2 of $-2.006\ s^{-1}$ for 10-nm nanoparticles and $-2.214\ s^{-1}$ for clusters, correlating with theoretical predictions and corresponding to the quadratic nature of diffusion distances versus time, whereby water molecules are expected to diffuse past small particles (<10 nm) more than an order of magnitude faster than 35-nm particles. Nonetheless, smaller particle sizes usually result in more efficient tissue clearance, and the effect on diffusing water molecules described here coincides with the overall applicability of biomedically relevant single nm SPIONs.[49,50] Some discrepancies could be a result of nano-scale and pico-scale variations in fabricated structures compared with chemical synthesis of SPIONs. The ability to determine precise peak R_2 values by nanopatterning diverse cluster topologies can drive the design of new sensor technologies for MRI. Our fabrication protocol could be expanded for patterning other particle material compositions and even patterning of widely used molecular agents. Broadening the scope of both native and modified nanoparticles for magnetic particle imaging,[51] optically detected MR,[52] and fluorescent imaging[53] could help optimize static and dynamic image contrast, SNR, and sensitivity to analytes without sacrificing

15222594, 2024, 2, Downloaded from https://onlinelibrary.wiley.com/doi/10.1002/mrm.29898 by Centura Health Library, Wiley Online Library on [29/11/2023]. See the Terms and Conditions (https://onlinelibrary.wiley.com/terms-and-conditions) on Wiley Online Library for rules of use; OA articles are governed by the applicable Creative Commons License

biocompatibility or resolution. Future experiments will consist of nanofabricating 2D and 3D array combinations composed of self-assembling modules with additional geometries to confirm that our work extends to three dimensions and performing multimodal magnetic imaging of array samples implanted in vivo. In conclusion, our analyses agree with and contribute further understanding into iron oxide nanoparticle aggregation-dependent field behavior observed in theoretical predictions. Our results lay a robust and adaptable foundation for the design and development of nanometer-scale and micrometer-scale contrast agents and probes for MRI and related modalities.

ACKNOWLEDGMENTS

The authors gratefully acknowledge the use of facilities and instrumentation supported by NSF through the University of Wisconsin Materials Research Science and Engineering Center (DMR-1720415) and thank Dr. Alan McMilllan for the useful advice about MR measurements. This work was supported by the National Institute of Neurological Disorders and Stroke and the Office of the Director's Common Fund at the National Institutes of Health (Grant DP2NS122605 to AH) and the National Institute of Biomedical Imaging and Bioengineering (Grant K01EB027184 to AH). This material is also based on research supported by the US Office of Naval Research under award numbers N00014-23–1-2006 and N00014-22–1-2371 to A.H. through Dr. Timothy Bentley and the Wisconsin Alumni Research Foundation (WARF).

ORCID

Ilhan Bok https://orcid.org/0000-0002-4481-7843
Aviad Hai https://orcid.org/0000-0002-4556-3048

TWITTER

Aviad Hai AviadHai

REFERENCES

1. Gleich B, Weizenecker J. Tomographic imaging using the nonlinear response of magnetic particles. *Nature.* 2005;435:1214-1217. doi:10.1038/nature03808
2. Graeser M, Thieben F, Szwargulski P. et al.Human-sized magnetic particle imaging for brain applications. *Nat Commun.* 2019;10:1936. doi:10.1038/s41467-019-09704-x
3. Barry JF, Turner MJ, Schloss JM, et al. Optical magnetic detection of single-neuron action potentials using quantum defects in diamond. *Proc Natl Acad Sci.* 2016;113:14133-14138. doi:10.1073/pnas.1601513113
4. Davis HC, Ramesh P, Bhatnagar A, et al. Mapping the microscale origins of magnetic resonance image contrast with subcellular diamond magnetometry. *Nat Commun.* 2018;9:131. doi:10.1038/s41467-017-02471-7
5. Wahsner J, Gale EM, Rodríguez-Rodríguez A, Caravan P. Chemistry of MRI contrast agents: current challenges and new frontiers. *Chem Rev.* 2019;119:957-1057. doi:10.1021/acs.chemrev.8b00363
6. Dadfar SM, Roemhild K, Drude NI, et al. Iron oxide nanoparticles: diagnostic, therapeutic and theranostic applications. *Adv Drug Deliv Rev.* 2019;138:302-325. doi:10.1016/j.addr.2019.01.005
7. Smith BR, Gambhir SS. Nanomaterials for in vivo imaging. *Chem Rev.* 2017;117:901-986. doi:10.1021/acs.chemrev.6b00073
8. Waddington DEJ, Boele T, Maschmeyer R, Kuncic Z, Rosen MS. High-sensitivity in vivo contrast for ultra-low field magnetic resonance imaging using superparamagnetic iron oxide nanoparticles. *Sci Adv.* 2020;6:eabb0998. doi:10.1126/sciadv.abb0998
9. Goodwill PW, Saritas EU, Croft LR, et al. X-space MPI: magnetic nanoparticles for safe medical imaging. *Adv Mater.* 2012;24:3870-3877. doi:10.1002/adma.201200221
10. Pouliquen D, Le Jeune JJ, Perdrisot R, Ermias A, Jallet P. Iron oxide nanoparticles for use as an MRI contrast agent: pharmacokinetics and metabolism. *Magn Reson Imaging.* 1991;9:275-283. doi:10.1016/0730-725X(91)90412-F
11. Reimer P, Müller M, Marx C, et al. T1 effects of a bolus-injectable superparamagnetic iron oxide, SH U 555 A: dependence on field strength and plasma concentration–preliminary clinical experience with dynamic T1-weighted MR imaging. *Radiology.* 1998;209:831-836. doi:10.1148/radiology.209.3.9844683
12. Zhang H, Guo Y, Jiao J, et al. A hepatocyte-targeting nanoparticle for enhanced hepatobiliary magnetic resonance imaging. *Nat Biomed Eng.* 2023;7:221-235. doi:10.1038/s41551-022-00975-2
13. Weissleder R, Stark D, Engelstad B, et al. Superparamagnetic iron oxide: pharmacokinetics and toxicity. *Am J Roentgenol.* 1989;152:167-173. doi:10.2214/ajr.152.1.167
14. Chertok B, Moffat BA, David AE, et al. Iron oxide nanoparticles as a drug delivery vehicle for MRI monitored magnetic targeting of brain tumors. *Biomaterials.* 2008;29:487-496. doi:10.1016/j.biomaterials.2007.08.050
15. Ferrucci JT, Stark DD. Iron oxide-enhanced MR imaging of the liver and spleen: review of the first 5 years. *Am J Roentgenol.* 1990;155:943-950. doi:10.2214/ajr.155.5.2120963
16. Neuwelt EA, Várallyay P, Bagó AG, Muldoon LL, Nesbit G, Nixon R. Imaging of iron oxide nanoparticles by MR and light microscopy in patients with malignant brain tumours. *Neuropathol Appl Neurobiol.* 2004;30:456-471. doi:10.1111/j.1365-2990.2004.00557.x
17. Hai A, Jasanoff A. Molecular fMRI. In: Toga AW, ed. *Brain Mapping*. Academic Press; 2015:123-129. doi:10.1016/B978-0-12-397025-1.00013-0
18. Lee N, Yoo D, Ling D, Cho MH, Hyeon T, Cheon J. Iron oxide based nanoparticles for multimodal imaging and magnetoresponsive therapy. *Chem Rev.* 2015;115:10637-10689. doi:10.1021/acs.chemrev.5b00112
19. Ghosh S, Harvey P, Simon JC, Jasanoff A. Probing the brain with molecular fMRI. *Curr Opin Neurobiol.* 2018;50:201-210. doi:10.1016/j.conb.2018.03.009
20. Atanasijevic T, Shusteff M, Fam P, Jasanoff A. Calcium-sensitive MRI contrast agents based on superparamagnetic iron oxide nanoparticles and calmodulin. *Proc Natl Acad Sci.* 2006;103:14707-14712. doi:10.1073/pnas.0606749103

15222594, 2024, 2, Downloaded from https://onlinelibrary.wiley.com/doi/10.1002/mrm.29898 by Centura Health Library, Wiley Online Library on [29/11/2023]. See the Terms and Conditions (https://onlinelibrary.wiley.com/terms-and-conditions) on Wiley Online Library for rules of use; OA articles are governed by the applicable Creative Commons License

21. Atanasijevic T, Jasanoff A. Preparation of iron oxide-based calcium sensors for MRI. *Nat Protoc.* 2007;2:2582-2589. doi:10.1038/nprot.2007.377
22. Okada S, Bartelle BB, Li N, et al. Calcium-dependent molecular fMRI using a magnetic nanosensor. *Nat Nanotechnol.* 2018;13:473-477. doi:10.1038/s41565-018-0092-4
23. Hsieh V, Okada S, Wei H, et al. Neurotransmitter-responsive nanosensors for T_2-weighted magnetic resonance imaging. *J Am Chem Soc.* 2019;141:15751-15754. doi:10.1021/jacs.9b08744
24. Narain R, Gonzales M, Hoffman AS, Stayton PS, Krishnan KM. Synthesis of monodisperse biotinylated p(NIPAAm)-coated iron oxide magnetic nanoparticles and their bioconjugation to streptavidin. *Langmuir.* 2007;23:6299-6304. doi:10.1021/la700268g
25. Perez JM, Josephson L, O'Loughlin T, Högemann D, Weissleder R. Magnetic relaxation switches capable of sensing molecular interactions. *Nat Biotechnol.* 2002;20:816-820. doi:10.1038/nbt720
26. Rodriguez E, Lelyveld VS, Atanasijevic T, Okada S, Jasanoff A. Magnetic nanosensors optimized for rapid and reversible self-assembly. *Chem Commun.* 2014;50:3595-3598. doi:10.1039/C4CC00314D
27. Chen KL, Mylon SE, Elimelech M. Enhanced aggregation of alginate-coated iron oxide (hematite) nanoparticles in the presence of calcium, strontium, and barium cations. *Langmuir.* 2007;23:5920-5928. doi:10.1021/la063744k
28. Zabow G, Dodd SJ, Koretsky AP. Shape-changing magnetic assemblies as high-sensitivity NMR-readable nanoprobes. *Nature.* 2015;520:73-77. doi:10.1038/nature14294
29. Nguyen T, Gao J, Wang P, et al. In vivo wireless brain stimulation via non-invasive and targeted delivery of magnetoelectric nanoparticles. *Neurother J Am Soc Exp Neurother.* 2021;18:2091-2106. doi:10.1007/s13311-021-01071-0
30. Kozielski KL, Jahanshahi A, Gilbert HB, et al. Nonresonant powering of injectable nanoelectrodes enables wireless deep brain stimulation in freely moving mice. *Sci Adv.* 2021;7:eabc4189. doi:10.1126/sciadv.abc4189
31. Bok I, Haber I, Qu X, Hai A. In silico assessment of electrophysiological neuronal recordings mediated by magnetoelectric nanoparticles. *Sci Rep.* 2022;12:8386. doi:10.1038/s41598-022-12303-4
32. Phillips J, Glodowski M, Gokhale Y, Dwyer M, Ashtiani A, Hai A. Enhanced magnetic transduction of neuronal activity by nanofabricated inductors quantified via finite element analysis. *J Neural Eng.* 2022;19:46003. doi:10.1088/1741-2552/ac7907
33. Hai A, Cai LX, Lee T, Lelyveld VS, Jasanoff A. Molecular fMRI of serotonin transport. *Neuron.* 2016;92:754-765. doi:10.1016/j.neuron.2016.09.048
34. Li N, Jasanoff A. Local and global consequences of reward-evoked striatal dopamine release. *Nature.* 2020;580:239-244. doi:10.1038/s41586-020-2158-3
35. Bricault S, Barandov A, Harvey P, DeTienne E, Hai A, Jasanoff A. Image-guided neural activity manipulation with a paramagnetic drug. *Nat Commun.* 2020;11:136. doi:10.1038/s41467-019-13933-5
36. Bok I, Vareberg A, Gokhale Y, et al. Wireless agents for brain recording and stimulation modalities. *Bioelectron Med.* 2023;9:20. doi:10.1186/s42234-023-00122-5
37. Muller RN, Gillis P, Moiny F, Roch A. Transverse relaxivity of particulate MRI contrast media: from theories to experiments. *Magn Reson Med.* 1991;22:178-182. doi:10.1002/mrm.1910220203
38. Brooks RA, Moiny F, Gillis P. On T_2-shortening by weakly magnetized particles: the chemical exchange model. *Magn Reson Med.* 2001;45:1014-1020. doi:10.1002/mrm.1135
39. Brooks RA. T(2)-shortening by strongly magnetized spheres: a chemical exchange model. *Magn Reson Med.* 2002;47:388-391. doi:10.1002/mrm.10064
40. Gillis P, Moiny F, Brooks RA. On T(2)-shortening by strongly magnetized spheres: a partial refocusing model. *Magn Reson Med.* 2002;47:257-263. doi:10.1002/mrm.10059
41. Matsumoto Y, Jasanoff A. T_2 relaxation induced by clusters of superparamagnetic nanoparticles: Monte Carlo simulations. *Magn Reson Imaging.* 2008;26:994-998. doi:10.1016/j.mri.2008.01.039
42. Jensen JH, Chandra R. Strong field behavior of the NMR signal from magnetically heterogeneous tissues. *Magn Reson Med.* 2000;43:226-236. doi:10.1002/(sici)1522-2594(200002)43:2<226::aid-mrm9>3.0.co;2-p
43. Yablonskiy DA, Haacke EM. Theory of NMR signal behavior in magnetically inhomogeneous tissues: the static dephasing regime. *Magn Reson Med.* 1994;32:749-763. doi:10.1002/mrm.1910320610
44. Sun N, Chen DX, Gu HC, Wang XL. Experimental study on T_2 relaxation time of protons in water suspensions of iron-oxide nanoparticles: waiting time dependence. *J Magn Magn Mater.* 2009;321:2971-2975. doi:10.1016/j.jmmm.2009.04.073
45. Choo ESG, Tang X, Sheng Y, Shuter B, Xue J. Controlled loading of superparamagnetic nanoparticles in fluorescent nanogels as effective T_2-weighted MRI contrast agents. *J Mater Chem.* 2011;21:2310-2319. doi:10.1039/C0JM03232H
46. Chen DX, Xu FJ, Gu HC. Experimental study on transverse relaxation rate of protons in water suspensions of magnetite nanoclusters: dependence of cluster sizes, volume fraction, inter-echo time, and waiting time. *J Magn Magn Mater.* 2012;324:2809-2820. doi:10.1016/j.jmmm.2012.04.016
47. Peng E, Wang F, Zheng B, Li SFY, Xue JM. Engineered water-soluble two-dimensional magnetic nanocomposites: towards highly magnetic relaxometric properties. *Nanoscale.* 2015;7:7819-7832. doi:10.1039/C5NR00810G
48. Zhou Z, Tian R, Wang Z, et al. Artificial local magnetic field inhomogeneity enhances T_2 relaxivity. *Nat Commun.* 2017;8:15468. doi:10.1038/ncomms15468
49. Wei H, Bruns OT, Kaul MG, et al. Exceedingly small iron oxide nanoparticles as positive MRI contrast agents. *Proc Natl Acad Sci.* 2017;114:2325-2330. doi:10.1073/pnas.1620145114
50. Kim BH, Lee N, Kim H, et al. Large-scale synthesis of uniform and extremely small-sized iron oxide nanoparticles for high-resolution T1 magnetic resonance imaging contrast agents. *J Am Chem Soc.* 2011;133:12624-12631. doi:10.1021/ja203340u
51. Ludwig F, Eberbeck D, Löwa N, et al. Characterization of magnetic nanoparticle systems with respect to their magnetic particle imaging performance. *Biomed Tech Eng.* 2013;58:535-545. doi:10.1515/bmt-2013-0013
52. Camarneiro F, Bocquel J, Gallo J, et al. Magnetic field mapping around individual magnetic nanoparticle agglomerates using nitrogen-vacancy centers in diamond. *Part Part Syst Charact.* 2021;38:2100011. doi:10.1002/ppsc.202100011
53. Yu Q, Zhang YM, Liu YH, Xu X, Liu Y. Magnetism and photo dual-controlled supramolecular assembly for suppression

15222594, 2024, 2, Downloaded from https://onlinelibrary.wiley.com/doi/10.1002/mrm.29898 by Centura Health Library, Wiley Online Library on [29/11/2023]. See the Terms and Conditions (https://onlinelibrary.wiley.com/terms-and-conditions) on Wiley Online Library for rules of use; OA articles are governed by the applicable Creative Commons License

of tumor invasion and metastasis. *Sci Adv.* 2018;4:eaat2297. doi:10.1126/sciadv.aat2297

SUPPORTING INFORMATION

Additional supporting information may be found in the online version of the article at the publisher's website.

Figure S1. Scanning electron microscope (SEM) images of developed poly methyl-methacrylate before iron oxide deposition. Shown are SEMs of representative hexagonal nanovoids patterned on poly methyl-methacrylate with $d_{pp}/r_p = 5$ (A), $d_{pp}/r_p = 10$ (B), and $d_{pp}/r_p = 20$ (C), and nanovoids with spacing $d_{pp}/r_p = 6$ (D), $d_{pp}/r_p = 8$ (E), and $d_{pp}/r_p = 10$ (F) (scale bars = 200 nm).

Figure S2. Linear fit of iron oxide nanostructure array optical image intensity. Box plot of optical image intensity (see square insets in upper right of Figure 2B) versus d_{pp}/r_p. Black dots denote the median; notches (present but not visible) denote bounds of statistical significance; and whiskers denote outlier thresholds (from $Q1 - W \times [Q3 - Q1]$ to $Q3 + W \times [Q3 - Q1]$ where $W = 1.5$). The orange line and data points represent a linear curve fit to the medians of each d_{pp}/r_p ($m = 1.6475 \times 10^5$ [optical intensity]/$[d_{pp}/r_p]^{-1}$, $b = 6.0603 \times 10^4$ [optical intensity], $p = 0$, one-way analysis of variance [ANOVA], $R^2 = 0.8915$).

How to cite this article: Bok I, Rauch B, Ashtiani A, Hai A. Direct observation of NMR transverse relaxation in nanopatterned clusters of iron oxide particles. *Magn Reson Med*. 2024;91:687-698. doi: 10.1002/mrm.29898

15222594, 2024, 2, Downloaded from https://onlinelibrary.wiley.com/doi/10.1002/mrm.29898 by Centura Health Library, Wiley Online Library on [29/11/2023]. See the Terms and Conditions (https://onlinelibrary.wiley.com/terms-and-conditions) on Wiley Online Library for rules of use; OA articles are governed by the applicable Creative Commons License